Compression Freezing Kinetics of Water to Ice VII

A. E. Gleason, C. A. Bolme, E. Galtier, H. J. Lee, E. Granados, D. H. Dolan, C. T. Seagle, T. Ao, S. Ali, A. Lazicki, D. Swift, P. Celliers, and W. L. Mao

1   **Compression freezing kinetics of water to ice VII**

2

3   **A.E. Gleason[1,2*], C.A. Bolme[1], E. Galtier[3], H.J. Lee[3], E. Granados[3], D.H. Dolan[4],**

4   **C.T. Seagle[4], T. Ao[4], S. Ali[5], A. Lazicki[5], D. Swift[5], P. Celliers[5], and W.L. Mao[2,6]**

5   [1]*Shock and Detonation Physics, Los Alamos National Laboratory, Los Alamos, NM*

6   *87545 USA*

7   [2]*Stanford Institute for Materials and Energy Sciences, SLAC National Accelerator*

8   *Laboratory, Menlo Park, CA 94025 USA*

9   [3]*Linac Coherent Light Source, SLAC National Accelerator Laboratory, Menlo Park, CA*

10   *94025 USA*

11   [4]*Sandia National Laboratories, Albuquerque, NM 87185 USA*

12   [5]*Shock Physics, Lawrence Livermore National Laboratory, Livermore, CA 94550 USA*

13   [6]*Geological Sciences, Stanford University, Stanford, CA 94305 USA*

14   PACS numbers: 64.70.dg, 64.60.Cn, 68.08.De

15   **Abstract**

16   Time-resolved X-ray diffraction (XRD) of compressed liquid water shows transformation

17   to ice VII in 6 nanoseconds, revealing crystallization rather than amorphous solidification

18   during compression freezing. Application of classical nucleation theory indicates

19   heterogeneous nucleation and one-dimensional (e.g., needle-like) growth. These first

20   XRD data demonstrate rapid growth kinetics of ice VII with implications for fundamental

21   physics of diffusion-mediated crystallization and thermodynamic modeling of

22   collisions/impact events on ice-rich planetary bodies.

23

24   **Background**

25   Understanding the phase diagram and properties of H_2O, a ubiquitous molecule in

26   the Universe and primary building block of icy satellites and water-rich exo-planets, is

27   crucial for physics and planetary science and has motivated studies on water under

28   extreme conditions for nearly a century [1]. It possesses a complicated high-pressure (P),

29   –temperature (T) phase diagram where high pressure phases exhibit novel phenomena

30   and intriguing properties, e.g., solid ice Ih having a lower density than liquid water, ice Ih

31   with an anomalous Clausius-Clapeyron slope, low-T, high-P polyamorphism [2], and a

32   superionic phase at ultra high pressure (e.g., Ref. [3]). Static- (e.g., Refs. [3-5]) and

33   dynamic-compression (e.g., Refs. [6-8]) experiments have been used to generate high-P

34   and/or –T conditions from which to study the complex H_2O phase diagram, chemical

35   properties and kinetics. Dynamic experimental platforms combined with optical

36   transmission and imaging provide insights into changes in state and phase at short

37   timescales [6,9]. In particular, quasi-isentropic dynamic compression, via reverberation

38   (multiple shock loading) or ramp-wave propagation, has been used to achieve high

39   pressure states at lower temperatures, allowing access to phases below the H_2O melt

40   boundary, such that the entropy is only slightly increased due to plastic work heating or

41   viscosity. Dolan *et al.* [10] observed liquid water to undergo a first order phase transition

42   using quasi-isentropic compression to a solid in less than 10 nanoseconds, but did not

43   have combined temporal and spatial resolution to extract information about the resultant

44   high-pressure phase and transformation mechanism. Similarly, Bastea *et al.* [11] explored

45   the kinetics of over-compressed water transforming to a solid using velocimetry

46   measurements combined with hydrocode simulations, finding the resultant high-pressure

47   phase properties most like ice VII. The fast mechanical loading of shockwaves as a

48   dynamic compression tool combined with ultrafast X-ray probes provide unique access to

49   material-based timescales revealing rapid disorder-to-order transitions in condensed

50   matter [12]. Here, with femtosecond XRD we provide an upper bound on the timescale

51   for compression-based freezing of water and establish heterogeneous nucleation of body-

52   centered-cubic crystalline structure, ice VII, at extreme conditions.

53

54   **Results**

55   Atomic structure measurements of quasi-isentropically compressed (see Fig. 1 of

56   Supplemental Material [13]) water were made using transmission *in situ* XRD with 7.6

57   keV X-rays from the X-ray Free Electron Laser (XFEL) at the Matter in Extreme

58   Conditions (MEC) end-station of the Linac Coherent Light Source (LCLS) (Fig. 1). This

59   ramp-style compression is achieved through temporally tailoring a drive laser that slowly

60   increases ablation energy over 15 ns. The target geometry consisted of a clamp-style

61   water containment approach [29]. Individual packages of sandwiched diamond – water –

62   quartz served as the target: [80 um thick <110> single-crystal diamond] + [155 um

63   deionized water (18 MOhm) layer set by a circular silicone washer (Silastic J, Dow

64   Corning)] + [40 um *c*-cut α-quartz]. A 75 nm gold layer served as the reflective layer for

65   velocimetry and as an internal pressure calibrant.

66   XRD from each pump-probe experiment, recorded on the Cornell-SLAC Pixel

67   Array Detectors (CSPADs), is azimuthally integrated (Fig. 2) as a function of X-ray

68   scattering angle (2θ) (see Methods). Ambient condition XRD patterns record the diffuse

69   scatter from the liquid water (between ~30-53° 2θ) plus three gold peaks. XRD

70   measurements are spatially integrated through the whole sample and therefore the

71   diffraction measures varying contributions from ambient and compressed target package

72   materials as a function of time due to the ramp-wave propagation. A relative time zero is

73   defined as the time when the ramp-wave enters the water. As the wave propagates

74   through the water, time-delayed diffraction, from 7.5 to 18.9 ns, shows compression of

75   the gold and emergence of two new peaks at ~40° and ~58° 2θ. These peaks shift to

76   slightly higher 2θ as the compression wave transits the sample and pressure increases.

77   The new peaks are indexed as high-pressure crystalline ice VII (body-centered cubic, Pn-

78    $3m$ used in the second origin setting in GSAS) [30]. The relative intensities of the first

79   two Bragg reflections (110) and (200) show no preferred orientation (i.e., comparable

80   relative intensities to Refs. [5,31]). Rietveld refinement is a powerful tool for quantitative

81   crystal structure analysis, widely used in the X-ray diffraction community. Our Rietveld

82   refinement parameters and example profile fit pattern are listed in Supp. Mat. Table 1 and

83   Fig. 2 inset, respectively. Pressures are derived from the peak positions of internal Au

84   calibrant. These pressures include a small (few percent) thermal correction due to heating

85   from quasi-isentropic compression [32,33]. We find excellent agreement between the

86   temperature corrected ice VII unit cell volume derived pressure and the internal Au

87   calibrant (Supp. Mat. Table 1), recording P, T conditions of ~2 GPa, 350 K to ~5 GPa,

88   400 K, Ref. [5]. The last two time-resolved traces, runs 132 and 136, did not contain

89   gold, therefore we estimate pressure using the ice VII unit cell volume. Our peak

90   positions do not match hexagonal ice VI, a candidate high pressure ice phase previously

91   observed at ~2 GPa, 350 K in static compression experiments [5]. Recent computational

92   work suggests rapid freezing of liquid water to a plastic ice phase with the same

93   translational order as ice VII, with the molecules rotating freely [34]. Our 2θ coverage

94   and peak intensity ratios do not allow us to distinguish between crystalline ice VII and

95   plastic ice.

96   Velocimetry data, recorded on the Velocity Interferometer System for Any

97   Reflector (VISAR) system, used the Au reflective surface and were collected

98   simultaneously with XRD (example run 130, Fig. 3); analysis given in Supplementary

99   Materials, Discussion 1. Due to shot-to-shot variation in VISAR quality and (possible)

100   issues of field-of-view alignment vs. X-ray probe, we use the velocimetry data only in the

101   capacity to compliment diffraction interpretation and not to strictly constrain pressures.

102   Indication of a velocity 'push-forward' at 3 ns or 6 ns (Fig. 3) corroborates the onset of a

103   phase transition to high pressure crystalline phase, resolvable in the XRD by 7.5 ns.

104   Moreover, VISAR measurements confirm the sample is not directly shocking from an

105   ambient to peak state – providing evidence that the temperatures are low enough to form

106   ice VII.

107   Individual liquid cell targets suited for high-repetition rate laser-shock are

108   technically challenging to design and fabricate. The clamp-style sealing mechanism

109   induces a level of contamination of the deionized water by the gasketing material, in this

110   case, silicone. Pre-shot fresh water filtration is not possible and a water sample is in

111   contact with silicone for 6-12 hours preceding the shot. We quantified the Si

112   contamination by radial diffusion from the silicone into deionized water using ICP-MS

113   (see Supplementary Methods, Discussion 2), finding the aqueous Si-species

114   concentration to be, at most, a few ppm.

115

116   **Discussion**

117   According to classical nucleation theory (e.g., Ref. [35]), the descriptions of

118   homogeneous and heterogeneous nucleation are similar. The transformation kinetics are

119   described by a rate equation, commonly referred to as the Johnson-Mehl-Avrami-

120   Kolmogorov (JMAK) model [36-38] for the transformed mass or volume fraction with an

121   exponential functional form:

122        $$\alpha(t) = 1 - \exp\left(-(k(t-\tau))^n\right) \qquad\qquad (1)$$

123   where $\alpha(t)$ is the fraction of the material transformed as a function of time, t; k is a

124   crystallization rate constant, τ, is incubation time, and *n is* the JMAK kinetic exponent.

125   The kinetic exponent contains contributions from nucleation probability and growth

126   topology. JMAK theory is traditionally applied to ambient pressure melt quench

127   experiments to extract details about the transformation mechanism, generally assuming a

128   random distribution of nucleation sites [39]. However, due to the destructive nature of a

129   dynamic-compression experiment, quantification of *in situ* phase transformed volume

130   fractions has not been possible until now. Using our time-resolved XRD of ice VII and

131   phase fraction analysis from Rietveld refinement, we examine the crystallization kinetics

132   of H_2O, providing insights for the basic mechanism of the transition during isentropic

133   compression (Fig. 4a). The mass fraction of ice VII as a function of time (Fig. 4b) for 7 –

134   13 ns is determined using the internal phase fraction marker method, e.g. Au layer,

135   (Supplementary Methods, Discussion 3), whereas the later two time slices (17-19 ns) do

136   not have an Au layer. These phase fractions were assessed using the sum of areas under

137   Gaussian fits to ice VII (110) and (200) peaks relative to total area under the trace with a

138   ~2-fold increase in the uncertainty relative to the internal marker method. The best-fit

139   parameters for the JMAK model to our data are $\tau = 6.4 \; (\pm 1.1)$ ns, $n = 0.6 \; (\pm 0.2)$, and $k =$

140    $0.010 \; (\pm 0.007)$ ns^{-1} (Fig. 4b, red curve). We investigate a range of parameter

141   combinations for comparison of goodness of fit (Fig 4b, grey curves and Supplementary

142   Method, Discussion 4). An incubation time of $\tau = 6.4$ ns for crystallization to begin is

143   representative of the first nucleation event(s) and fast for a disorder-to-order transition.

144   Dolan and Gupta [7] extrapolate an incubation time of 7 ± 2 ns at 5 GPa which is in

145   excellent agreement with this work. A JMAK kinetic exponent of 1 is typically the lower

146   bound for heterogeneous nucleation corresponding to nucleation on surfaces of, in this

147   case, Si impurities [40,41]. Due to our impurity level, homogeneous would not be

148   realistic since the presence of even trace amounts of Si would likely catalyze growth of

149   small ice grains and lower the free energy barrier for crystallization. This finding is

150   reinforced by Sun *et al*. [42] who demonstrate that the more inhomogeneous the

151   distribution of nucleation sites, the lower the JMAK kinetic exponent – which could

152   indicate our Si impurities are not uniformly disbursed. Therefore, our incubation time is

153   an upper limit demonstrating how fast nucleation can proceed due to the presence of a

154   spatially heterogeneous distribution of ppm impurities. More recently, $n \leq 1$ is thought to

155   be indicative of diffusion-controlled crystallization and heterogeneous, likely

156   simultaneous, nucleation [43]. This fast crystallization rate may support a one-

157   dimensional grain growth geometry, as in needles or rods [43,44]. Admittedly, JMAK

158   theory is phenomenological and may not be ideal for all dynamic compression datasets,

159   yet in the absence of a more exact kinetics model available at this time we rely on the

160   JMAK basic functional form to give a qualitative, physical picture of transformation [39].

161   Moreover, this new experimental platform enables high-spatial and –temporal fidelity

162   XRD from which phase fraction extraction can encourage the kinetics modeling

163   community to make advancements.

164   Direct observations of ice VII formation under ramp-compression have

165   implications ranging from fundamental physics of diffusion-mediated primary

166   crystallization to modeling of constituent planetary materials. In particular, we show that

167   dynamic phase transformations can result in crystallization (also e.g., Ref. [12]), not

168   necessarily amorphization. In the context of ice phases present in icy moons and extra-

169   solar planetary bodies, evaluation of extreme condition behavior of impurity-laden ices is

170   critical for modeling of planetary interiors [45]. The mechanical and thermodynamic

171   work from an impact event is typically derived from a material's shock Hugoniot

172   describing dynamic strength and phase properties [46] – yet until now direct, lattice-level,

173   time-resolved structural information approaching theoretical time-scales was not

174   available to validate optical transmission- or velocimetry-based measurements. Here we

175   see an almost immediate transformation to a high pressure ice-slush (i.e., water-ice VII

176   mixture). Compared to ice VII alone, this would effectively reduce the bulk modulus of

177   the mixed phase system and lead to rapid loss of strength during the initial stages of an

178   impact event. These new kinetics data could be used in modeling collisions onto and

179   between ice-rich planets and cometesimals in the outer solar system and provide more

180   information to understand the structure and petrology of their interiors.

181

182   **Methods**

183   Quasi-monochromatic (dE/E=0.2-0.5%), fully transverse coherent, 7.603(30) keV

184   x-ray pulses of 40 fs duration with an average of ~10^{12} photons per pulse, were incident

185   over a 50 μm diameter spot on the target package. An X-ray only shot was collected

186   before each drive shot as a reference. The 50 μm XFEL beam spot did not produce any

187   observable x-ray damage to the target. Metal coatings on the diamond ablator served to

188   absorb the drive laser (150 nm Al on upstream side) and act as the reflective layer for

189   velocimetry measurements (75 nm Au on downstream side).

190   The optical drive laser was defocused to a 250 μm diameter spot at FWHM with a

191   Gaussian spatial profile to achieve focal spot intensity of $\sim 10^{12}$ W/cm^2. The angle

192   between drive laser arms and XFEL probe was 22°. An ablation-driven compression

193   wave was launched parallel to the sample normal over a 15.0 ns ramp pulse profile

194   (Supplemental Fig. 1) from a frequency doubled Nd:Glass laser system (λ=527 nm). The

195   optical laser and x-ray beam were spatially overlapped and operated in single shot mode.

196   The absolute time zero corresponds to overlap of their leading edges. For each shot, a

197   time delay was selected for the XFEL pulse relative to the optical laser pulse with a jitter

198   of 0.35 ns. We establish a relative time zero defined as the time at which the pressure

199   wave reaches the interface between the diamond and the water, where the transit time

200   through the single crystal diamond is 4.40(35) ns, Ref. [47]. The pump-probe delay scans

201   at several nanosecond intervals enabled collection of a time-series of XRD patterns in

202   transmission geometry. XRD patterns were captured by Cornell-SLAC Pixel Array

203   Detectors (CSPADs) constructed of individual application-specific integrated circuits

204   (ASICs) [48]. Maximum azimuthal angle coverage was 230°, however due to the

205   mosaicked nature of the CSPADs, continuity of ice VII Debye rings was not possible

206   over this range. Integrated data was collected over an 80° azimuthal range. One target

207   was shot per time delay selected.

208   Using General Structure Analysis System (GSAS) software [30] with EXPGUI

209   [49], we perform Rietveld refinements on all integrated diffraction data (starting

210   crystallographic information file from Kamb and Davis [31]); an example is shown for

211   run 130, inset of Fig. 2. Pixels associated with the spaces in between ASICs of the

212   CSPADs have been removed for refinement. The goodness-of-fit factor (reduced-χ^2) and

213   lattice parameter (a) and unit cell volume (V) for each trace derived from each fit are

214   listed in Supplementary Materials Table 1.

215

216   Author to whom correspondence and requests for materials should be addressed:

217   Arianna Gleason <arianna@lanl.gov>

218

219

220

221

222

223

224

225

226

227

228

229

230

231   **Figures:**
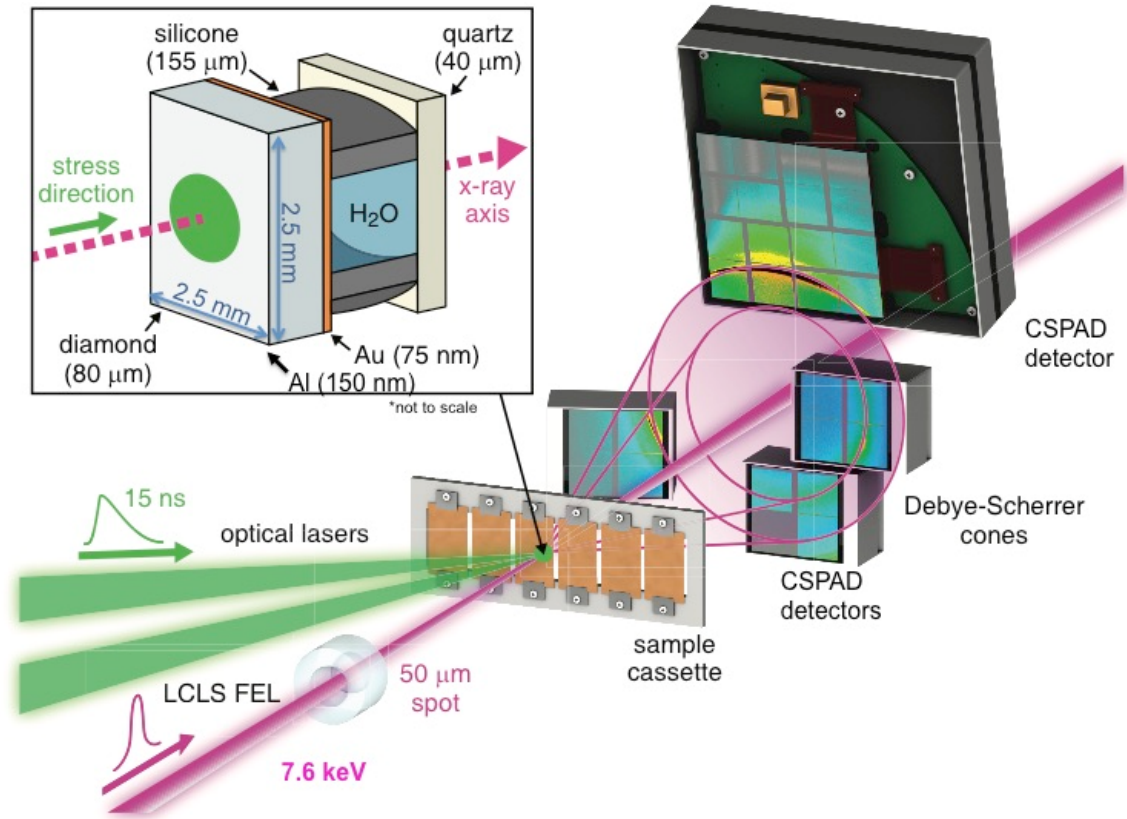
232

233   FIG. 1. Experimental configuration of the XFEL probe and optical laser. The shock

234   freezing behavior of water captured in a Debye-Scherrer geometry. *Inset:* Schematic of

235   target package as a cut away side-view.

236

237

238
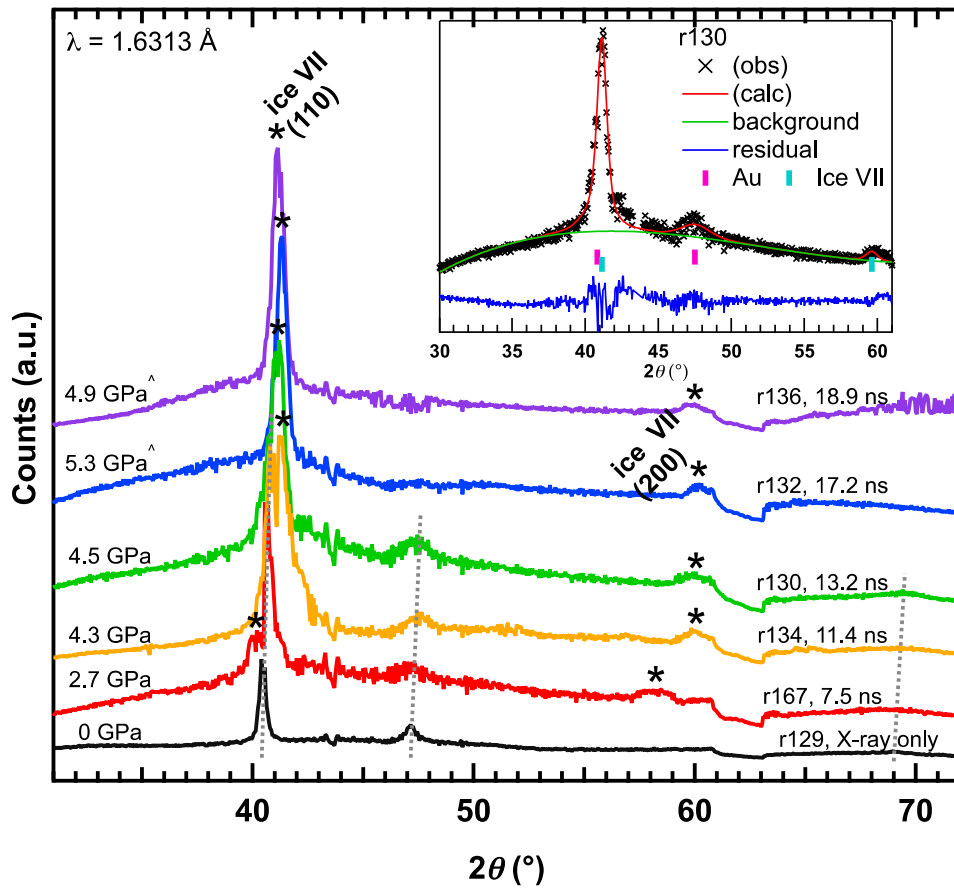
FIG. 2. Multiplot of time-resolved X-ray diffraction data. Dark subtracted raw diffraction

data plotted without any additional normalization. Traces are offset for visual clarity. Ice

VII (110) and (200) peaks are marked with asterisks. Au (111), (200) and (220) peak

position trends are marked with dashed grey lines. Au is used to estimate pressure for

traces between 7.5 - 13.2 ns (Refs. [32,33]). Samples for the last two traces, 17.2 and 18.9

ns, did not have an Au coating, therefore pressures (denoted with ^) are estimated from

the ice VII equation of state [5]. Breaks in the detector are seen at 2θ of 43.5°, 49.5° and

61°. *Inset:* Example of Rietveld refinement performed on Run 130 showing good

agreement between the observed and calculated patterns.

248

249
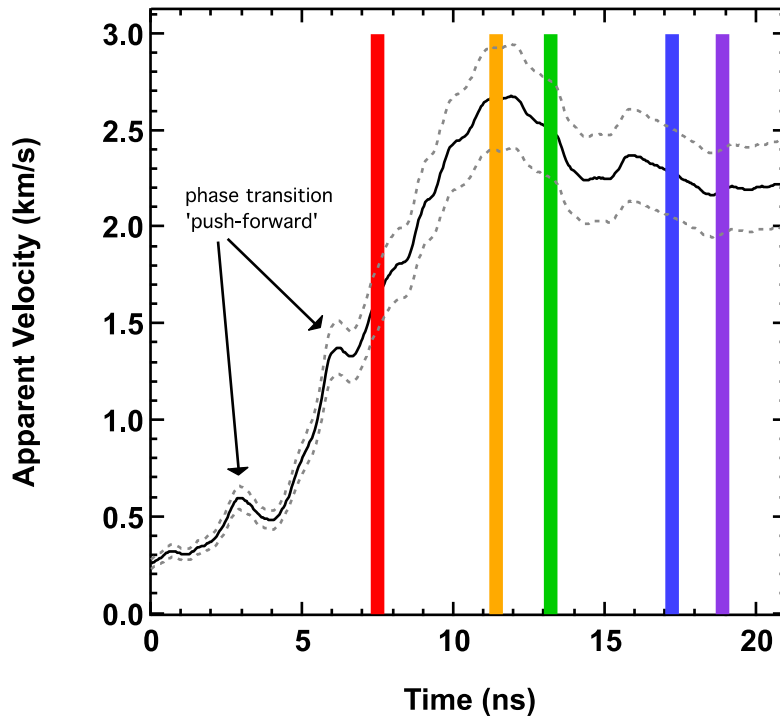
FIG. 3. VISAR spatially averaged lineout. An average of the central 100 μm region of

the apparent velocity histories. Colored bars (matched to Fig. 2 traces) indicate XFEL

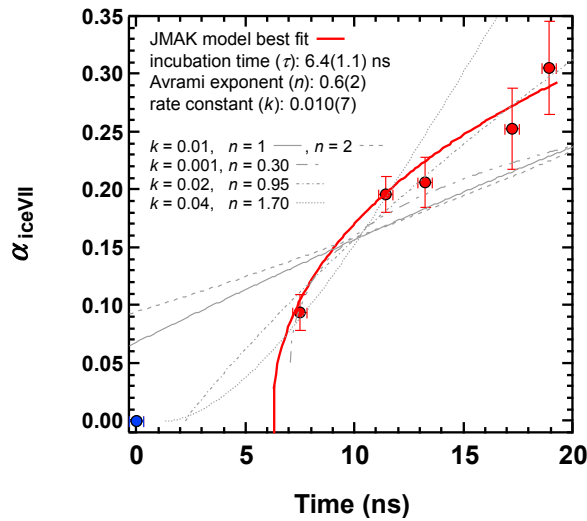probe time where width of the bar includes the +/- 350 ps timing uncertainty.

253

254

255
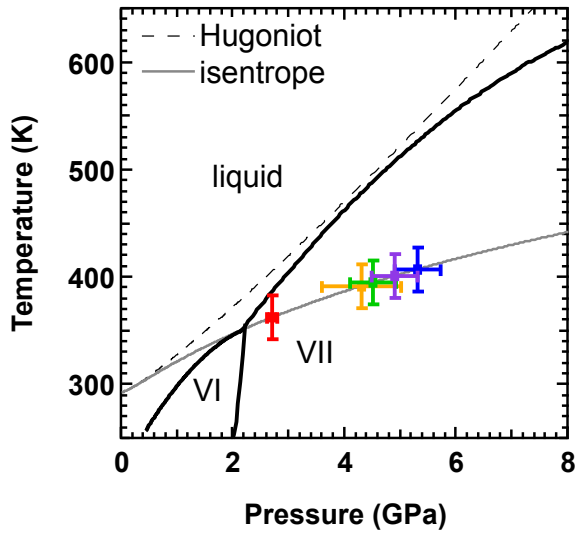
256   a.

257   b.

FIG. 4. Phase diagram of H_2O and trend in volume fraction converted to ice VII in

explored phase-space. (a) Equilibrium phase diagram of H_2O (Ref. [50]) and Hugoniot

(dashed trace) and isentrope (grey trace) curves from IAPWS95 liquid equation of state

[32]. Colored points show coverage of phase space accessed in this work with the (b)

fraction converted to ice VII ($\alpha_{ice\ VII}$, red points; blue point is starting time-zero fraction,

not included in the fit). Best JMAK model fit (red curve) is compared to other

combinations of JMAK parameters (grey curves).

265

266   **References**

267   [1] P. Bridgeman, Proc. Am. Acad. Arts Sci. **74,** 399 (1942).

268   [2] O. Mishima and E. Stanley, Nature **396**, 329 (1998).

269   [3] A. Goncharov *et al.*, Phys. Rev. Lett. **94**, 125508 (2005).

270   [4] R. Hemley *et al.,* Nature **330,** 737 (1987).

271   [5] L. Bezacier *et al.,* J. Chem. Phys. **141,** 104505 (2014).

272   [6] S. Kormer, K. Yushko and G. Krishkevich, Soviet Phys. Jetp **27,** 879 (1968).

273   [7] D. Dolan and Y. Gupta, J. Chem. Phys. **121,** 9050 (2004).

274   [8] S. Stewart and T. Ahrens, J. Geophys. Res. **110**, E03005 (2005).

275   [9] D. Dolan, J. Johnson, and Y. Gupta, J. Chem. Phys. **123,** 064702 (2005).

276   [10] D. Dolan, M. Knudson, C. Hall, and C. Deeney, Nat. Phys. **3**, 339 (2007).

277   [11] M. Bastea, S. Bastea, J. Reaugh and D. Reis, Phys. Rev. B **75**, 172104 (2007).

278   [12] A. Gleason *et al.*, Nat. Comm. **6**, 8191 (2015).

279   [13] See Supplemental Material at http://xxx , which includes Refs. [14-28], for more

280   details concerning drive profile, Lagrangian stress tracer plot, unit cell and fit parameters

281   for Rietveld refinements of Au and ice VII, and discussions of water sample purity,

282   VISAR analysis, phase fraction assessment strategies, and JMAK model fit parameters.

283   [14] D. Bloomquist and S. Sheffield, J. Appl. Phys. **54**, 1717 (1983).

284   [15] P. Celliers, D. Bradley, G. Collins, D. Hicks, T. Boehly, and W. Armstrong, Rev.

285   Sci. Instru. **75**, 4916 (2004).

286   [16] T. Ao, Sandia Report no. SAND2009-3236, 2009.

287   [17] M. Takeda, J. Ina, and S. Kobayashi, J. Optic. Soc. Am. **72**, 156 (1982).

288   [18] W. Macy, Appl. Opt. **22,** 3898 (1983).

289   [19] D. Dolan, Ph.D. Thesis, Washington State University, 2003.

290   [20] H. Shimizu, T. Nabetani, T. Nishiba, and S. Sasaki, Phys. Rev. B **53**, 6107 (1996).

291   [21] M. Lang *et al.,* J. Mater. Res. **24,** 1322 (2009).

292   [22] A. Gualtieri, A. Guagliardi, and A. Iseppi, A. The quantitative determination of the

293   crystalline and the amorphous content by the rietveld method: application to glass

294   ceramics with different absorption coefficients. *Diffraction analysis of the*

295   *microstruct.ure of materials.* (Springer-Verlag, Berlin, 2004).

296   [23] R. Snellings, L. Machiels, G. Mertens, and J. Elsen, Geologica Belgica **13,** 183

297   (2010).

298   [24] J. Malek, Thermochimica Acta **267,** 61 (1995).

299   [25] E. Dill, J. Folmer, and J.Martin, Chem. Mater. **25**, 3941 (2013).

300   [26] M. Bastea, S. Bastea, J. Reaugh, and D. Reisman, Phys. Rev. B **75**, 172104 (2007).

301   [27] D. Barahona, Atmos. Chem. Phys. **15**, 13819 (2015).

302   [28] M. Bastea, S. Bastea, S., and R. Becker, Appl. Phys. Lett. **95**, 241911 (2009).

303   [29] S. Ali Gordon Research Conference, High Pressure Conf. Board 1-24, ID 1281151

304   (2012).

305   [30] A. Larson and R. Von Dreele, Los Alamos National Laboratory Report, LAUR 86-

306   748 (2000).

307   [31] B. Kamb and B. Davis, Proc. Natl. Acad. Sci. **52**, 1433 (1964).

308   [32] W. Wagner and A. Pruβ, J. Phys. Chem. Ref. Data **31,** 387 (2002).

309   [33] Y. Fei, A. Ricolleau, M. Frank, K. Mibe, G. Shen, and V. Prakapenka, Proc. Natl.

310   Acad. Sci. USA **104**, 9182 (2007).

311   [34] J. Aragones and C. Vega, J. Chem. Phys. **130,** 244504 (2009).

312   [35] J. Christian, J. *The theory of transformations in metals and alloys.* (2nd Edn.

313   Pergamon, New York, 1975).

314   [36] A. Kolmogorov, Izv. Akademii Nauk USSR Ser Matematic **3,** 355 (1937).

315   [37] W. Johnson and R. Mehl, Trans. AIME **125,** 416 (1939).

316   [38] M. Avrami, J. Chem. Phys. **7**, 1103 (1939).

317   [39] P. Bruna, D. Crespo, R. Gonzalez-Cinca and E. Pineda, J. Appl. Phys. **100**, 054907

318   (2006).

319   [40] T. Kruger, B. Merkau, W. Grosshans, and W. Holzapfel, High Press. Res. **2,** 193

320   (1990).

321   [41] N.V.C. Shekar, N.V.C. and G. Rajan, Bull. Mater. Sci. **24**, 1 (2001).

322   [42] N. Sun, X. Liu and K. Lu, Scripta Materialia 34, 1201-1207 (1996).

323   [43] J. Lopes-da-Silva and J. Coutinho, Energy & Fuels **21**, 3612 (2007).

324   [44] M. Talukdar and P.G. Achary, IJRRAS **3**, 92 (2010).

325   [45] M. Frank, H. Scott, E. Aarestad, and V. Prakapenka, Geochimica et Cosmochimica

326   Acta **174,** 156 (2016).

327   [46] L. Senft and S. Stewart, J. Geophys. Res. **112,** 1 (2007).

328   [47] R.S. McWilliams *et al.,* Phys. Rev. B **81**, 014111 (2010).

329   [48] H. Philipp, M. Hromalik, M. Tate, L. Koerner, and S. Gruner, S. Nat. Synchrotron

330   Rad. Instru. **649**, 67 (2011).

331   [49] B.H. Toby, J. Appl. Cryst. **34**, 210 (2001).

332   [50] C. Pistorius, E. Rapoport, and J. Clark, J. Chem. Phys. **48,** 5509 (1968).

333

334

Author contributions

C.B. participated in the experiment and developed XRD projection software. E.Ga., H.J.L., and E.Gr. participated in the experiment as MEC instrument scientists and contributed to data interpretation. D.D., T.A. and C.S. contributed to interpretation and provided VISAR modeling/interpretation. W.M., S.A., A.L., D.S., and P.C. contributed to data collection. A.G. was principal investigator, analyzed the data, and wrote the paper.

Competing financial interests

The authors declare no competing financial interests.